Berlin Beamforming Conference

A LAPLACIAN FILTERING-BASED TECHNIQUE TO LOCALIZE VORTEX SHEDDING NOISE IN A STRONGLY CONTAMINATED ENVIRONMENT

Esztella Balla[1] and János Vad[1]
[1]Budapest University of Technology and Economics, Faculty of Mechanical Engineering,
Department of Fluid Mechanics
Bertalan Lajos utca 4-6., 1111, Budapest, Hungary

ABSTRACT

Phased array microphone measurements are performed in order to localize the origin of profile vortex shedding, and to detect trailing edge bluntness noise. Individual blade sections, characteristic of low-speed axial fans are examined at various angles of attack and wind speeds. The measurements are corrupted with reverberations and high background noise, resulting in low signal-to-noise ratio. A processing technique, based on Laplacian filtering is proposed to obtain meaningful results from the highly contaminated data. According to the results, the proposed technique is capable of detecting sources of vortex shedding from measurements with low signal-to-noise ratio. The results are in accordance with the trends established in the literature from qualitative, and to a limited extent, from quantitative points of view. For validation purposes supplementary hot wire measurements are utilized. The trailing edge bluntness noise, of known position was used to judge the localization capabilities of the microphone array measurements, together with the processing technique.

1   INTRODUCTION

The aim of this paper is to propose a novel measurement technique, for the identification of vortex shedding noise from low-speed axial fan blade sections. At low Reynolds numbers the aerodynamic behavior of blades differs significantly from the behavior at higher Reynolds numbers. The limiting Reynolds number, below which aerodynamic changes start to take effect, is $Re \approx 150\,000$, according to the literature [1]. The Reynolds number is defined based on the chord of the profile, i.e. $Re = cU/v$, where c is the chord, U is the free-stream velocity, and v is the kinematic viscosity of the fluid. Simpler, non-profiled, e.g. cambered plates with circular arc camber line, may perform aerodynamically better, i.e. have a higher lift-to-drag ratio. The blading of fans can be modelled with blade-sections, in a two-dimensional view, in the design phase. As suggested by [2], detailed acoustic measurement data obtained for basic two-

dimensional (2D), rectilinear models of blade sections can be adapted to rotating blades, by means of a spanwise segment splitting. Thus the 2D modelling can be applied for both the aerodynamic and aeroacoustic design.

Axial ventilating fans are widely used in the close vicinity of humans, e.g. cooling fans, so their noise emission may have a negative effect on human comfort and health. These fans are often characterized by small size and/or low rotational speed, i.e. they work in the low Reynolds number regime. The noise of ventilating fans may originate from mechanical or aerodynamic sources. The aerodynamic noises can be classified into several categories, one of them is the blade self-noise. This category includes noise that is due to the interaction between the blade and the turbulence produced in its own boundary layer and near wake [3]. Self-noise can further be classified, based on the generating mechanisms. According to [4], one type of prominent blade self-noise, in case of low-speed axial fans, is the profile vortex shedding (PVS). PVS is the periodic shedding of coherent vortices over the lifting surface of the blade. Based on [5] PVS can cause up to 10 percent change in the lift coefficient of blades, which implies vibration issues, besides the produced noise. The noise production is linked to the global loss of the fan [6], and as such, noise reduction may bring a gain in fan efficiency. The findings presented herein are also applicable to the wings of micro-air vehicles, as they operate in a similar, low Reynolds number range.

With low computational cost, i.e. using Reynolds-averaged Navier-Stokes equations, Computational Fluid Dynamics (CFD) it is still cumbersome to predict the exact behavior of the boundary layer developing around blades. However, from the viewpoint of PVS it is of importance to precisely predict the laminar-turbulent transition of the boundary layer, and the reattachment. Consequently aerodynamic and aeroacoustic measurements still remain competitive compared to CFD.

The exact location of the origin of PVS is still under investigation in the literature [7]. The present paper aims to add to the open literature by providing information on blade sections characteristic of low-speed axial fans, namely a cambered plate and the RAF6-E profile, which is a representative case study for profiled blades. Although not used in fan design, results for a flat plate are also presented herein as reference.

The phased array microphone (PAM) technique offers a potential to determine the spatial location of the origin of PVS. Even nowadays, the PAM technique is relatively sensitive to background noise levels. This necessitates the development of techniques capable of obtaining meaningful acoustical results from measurements made under harsh conditions. In the field of image processing, great advance has already been achieved by using image processing algorithms [8, 9]. One of them is the Laplacian filtering technique [10], of which the authors wish to take advantage of.

In this paper a novel technique, based on the Laplacian filtering, will be presented for the processing of beamforming maps, contaminated with high background noise. The capabilities of the method are presented on a case study, including three different axial fan blade sections, within a Reynolds number range between 60 000 and 140 000. The signs of PVS and trailing edge vortex shedding noise, of known chordwise location, are searched for. The results are supported by hot-wire measurements, reported in [11], regarding the frequency of the vortex shedding, as well.

2   MEASUREMENT SETUP

The measurements were performed in the Blackbird 2 wind tunnel of the Department of Fluid Mechanics, Faculty of Mechanical Engineering, Budapest University of Technology and Economics. The arrangement of the wind tunnel is shown in Figure 1. The wind tunnel was originally designed for aerodynamic measurements, thus it lacks any additional acoustic treatment. The length and the height of the test section is 1m, and its width is 0.15 m. Originally the test section is closed from two sides. In order to enable acoustic access, one of the side walls was replaced with Kevlar fabric.
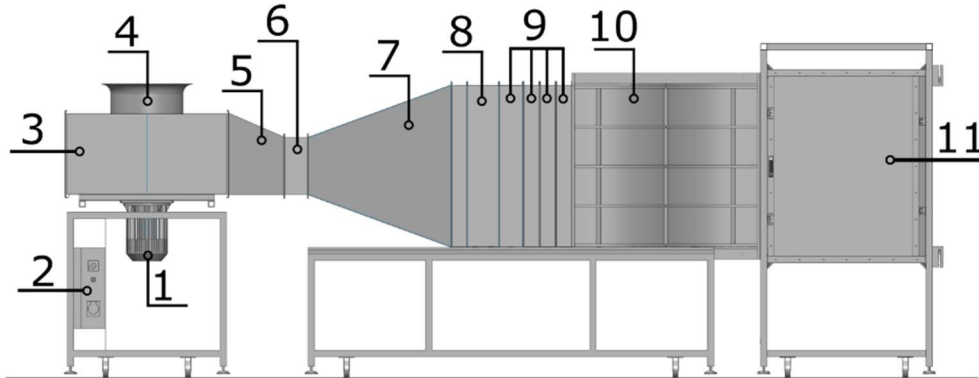
Figure 1. Measurement setup [12]. 1: Motor, 2: Frequency converter, 3: Radial fan, 4: Inlet bell mouth, 5: Guide vanes, 6: Flexible connector, 7: Split diffuser, 8: Honeycomb, 9: Turbulence reduction screens, 10: Transition element, 11: Test section

The acoustic measurements were performed with an OptiNav Inc. Array24 general purpose PAM. The array includes 24 microphones, placed in a logarithmic spiral. The aperture of the array is 1m. The sound recording interval was 30s, at a sampling frequency of 44.1kHz. The distance between the PAM and the midspan of the profiles was 0.4m. Besides the measurements on the profiles, background measurements were also performed, without the profiles at a running wind tunnel. The source strength data, gained from the measurements on the profiles, and on the background, will be denoted by SS_{PF} and SS_{BG}, respectively.

The profiles under investigation are shown in Figure 2. The geometrical data of the profiles are summarized in Table 1, where c is the chord, S is the span, t is the thickness, and h is the maximum height of the camber line. Each profile is equipped with a handle, with which it can be mounted into the built-in protractor of the test section. The set angles of attack were between 0°and 6°, with 2° steps. Measurements were made at three Reynolds numbers: 60 000, 100 000 and 140 000.
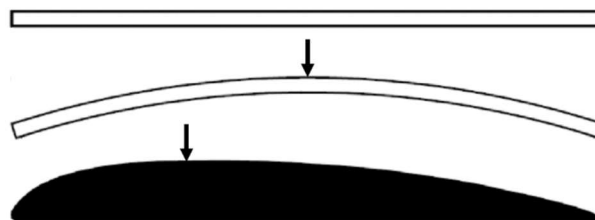

Figure 2. Cross-sections of the profiles. Flat (top), cambered (middle), airfoil (bottom). The arrows indicate the locations of the maximum height of the camber line.

Table 1. Geometrical data of the profiles

Profile	$c\ [mm]$	$S\ [mm]$	$t\ [mm]$	$h\ [mm]$
Flat	100	150	2.5	0
Cambered	100	150	2	8
Airfoil	100	150	10*	5
*maximum thickness				

3   PROCCESSING TECHNIQUE

For the evaluation of the measurements, the imageJ image-processing program with Beamform Interactive plug-in of OptiNav, and Matlab R2017a were used. As already discussed in [13], during the beamforming process, the diagonal of the cross spectral matrix was left untreated. As signs of vortex shedding were searched for, dipole noise character was assumed. According to [14, 15], using monopole beamforming for dipole type noise sources, may cause significant error in the results. The amount of the error is dependent on the directivity of the dipole [16]. In order to avoid these errors, time domain, dipole beamforming was applied to the measurements, the axis of the dipole was set normal to the chord line of the profiles.

Due to high background noise levels, background subtraction was necessary to obtain meaningful results. Before the subtraction, preliminary preparation of the data was needed. To achieve this, the following actions were taken: spatial confinement of the data, using the so called region of interest (ROI), and conversion. The conversion is applied only to the SS_{PF} measurements. The conversion is necessary, as in some cases the background noise level is higher in several points of the investigated domain, than the measurements with the profiles, i.e. $SS_{BG} > SS_{PF}$. The application of the conversion factor makes a logarithmic level representation over the entire ROI possible. The conversion factor, C was set by such means that the mean value of the result of background noise subtraction SS_{sub} over the boundary of the ROI is 1, corresponding to a 0 dB reference level. The conversion and the background subtraction is applied in the following manner:

$$SS_{sub} = C \cdot SS_{PF} - SS_{BG} \tag{1}$$

Fake sources may appear in the SS_{sub} map, being physically irrelevant to the noise originating from the profile. Such fake sources may be a cause of the following circumstances. a) Measurement error of the microphones. b) Perturbations of the background, potentially remaining even after background noise subtraction, e.g. reflections. c) Anomalies in the beamforming technique, e.g. side lobes. d) Limited spatial resolution of the PAM technique, falsifying the determination of the spatial extension of the noise sources. In what follows, a technique is proposed and demonstrated for attenuating the adverse effect of such fake sources in evaluation of the SS_{sub} results.

As discussed in detail in [13] the sound field has to be filtered in two ways, with low- and high-pass filtering. Low-pass filtering can be fulfilled by applying the Laplace equation on the domain:

$$\frac{\partial^2 SS_{sub}}{\partial x^2} + \frac{\partial^2 SS_{sub}}{\partial z^2} = 0 \tag{2}$$

where x and z are the streamwise and transversal coordinates, respectively. As the domain is discrete, Eq. (2) should be written in the following discretized form:

$$SS_{sub}(x_i, z_i) := \frac{1}{4}\{SS_{sub}(x_i + \Delta d, z_i) + SS_{sub}(x_i - \Delta d, z_i) + SS_{sub}(x_i, z_i + \Delta d) +$$
$$+SS_{sub}(x_i, z_i - \Delta d)\} \tag{3}$$

where i is the index of the grid point, and Δd is the spacing of the ROI computational grid.

The high-pass filtering is realized by appropriate boundary conditioning, which is also in accordance with the previously described conversion. The following boundary condition is prescribed for the grid points fitting to the rectangular boundary of the ROI:

$$SS_B \equiv 1 \tag{4}$$

By means of this constant boundary condition, it is declared that no separate, profile-related, point-like noise sources are distinguished at the boundary. The implementation of Eq. (3) to the ROI grid is carried out as follows. Starting from the corner points, the grid points of the adjacent grid lines are treated, starting with the rectangular line next to the boundary, and ending with the central straight, linear section.

The Laplacian filtering technique was applied multiple times in order to achieve the adequate amount of filtering. Attention had to be paid to determine the number of filtering iteration in a way that fully utilizes the perturbation-eliminating capabilities of the filtering technique, while minimizing the loss of information. The following filtering phases are distinguished:

- *underfiltered*: the noise maps are highly contaminated by extraneous perturbations,
- *optimum filtered*: the perturbations are minimized, while the noise source of interest is only moderately distorted,
- *overfiltered*: perturbations disappear, however the noise source of interest is also highly distorted,
- *fully overfiltered*: all case specific characteristics disappear, no meaningful information is left.

First, *overfiltering* was applied to all measurement cases. The value of the peak intensity, $SS_{sub,max}$, the position of the peak intensity in the streamwise and transversal directions, x_{max} and z_{max} respectively, and the transversal size of the -3dB contour from the peak, d_z were monitored. The convergence of these values for a representative example, the RAF6-E airfoil, at $Re = 100\ 000$, at angle of attack, $\alpha = 2°$, are shown in Figure 3. For better visibility the z_{max} and d_z values are multiplied by two in the figure, and $SS_{sub,max}$ has a separate axis. n is the number of Laplacian filtering cycle.

Then, starting again from an *underfiltered* state, filtering was carried out until the point where the peak position curve, converging to the final value has maximum gradient. The point of maximum gradient corresponds to the point of maximum possible deviation, nevertheless, as it will be seen later from the results, the average deviation and the overall localization capability of the method is retained. At this point the *overfiltered* region is not yet reached, however the filtering potential is taken advantage of completely, this is the state of *optimum filtering*. The maximum gradient point is reached at approximately the same iteration step for all monitored values. The point of maximum gradient is indicated with the dashed line, denoted by c). The beamforming maps, corresponding to different states of filtering, indicated with the dashed lines in Figure 3, are shown in Figure 4. The profile is represented with its chord only.

The contour lines indicate -1dB change, and the black cross is at the peak intensity. Before reaching the *optimum filtered* state the peak intensity, and its position relative to the trailing edge does not change significantly compared to the *underfiltered* cases. It can be seen that in the region of *overfiltering* the intensity levels decrease drastically from 73 dB to 45.5 dB, which corresponds to only 0.2% of the intensity of the *underfiltered* case, this means that all information on the intensity is practically lost. The position of the peak also changes relative to the trailing edge, causing information loss in the localization as well. Besides, also the shape of the contours change, compared to the *underfiltered*, and *optimum filtered* results, reaching gradually the *fully overfiltered* shape.
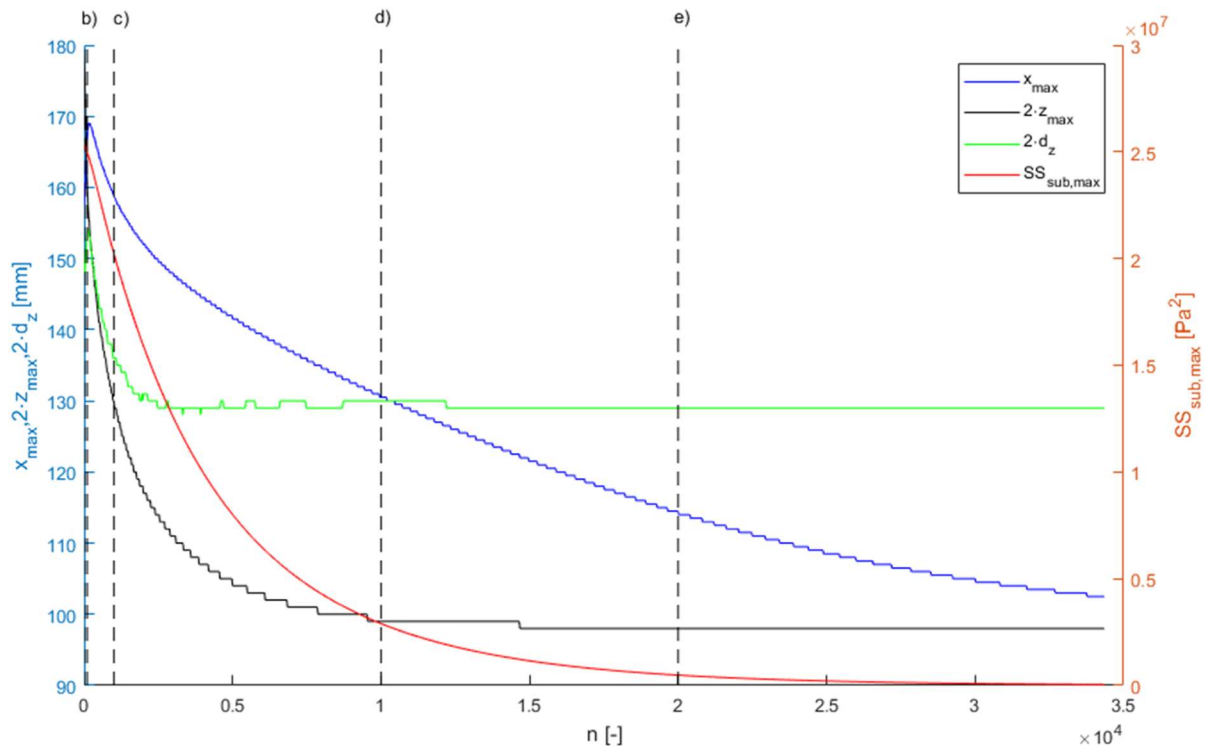
Figure 3. Convergence of x_{max}, z_{max}, d_z and $SS_{sub,max}$ as a function of Laplacian filtering number, for the RAF6-E airfoil at Re= 100 000 and α=2°. For better visibility the z_{max} and d_z values are multiplied by two in the figure, and $SS_{sub,max}$ has a separate axis

6
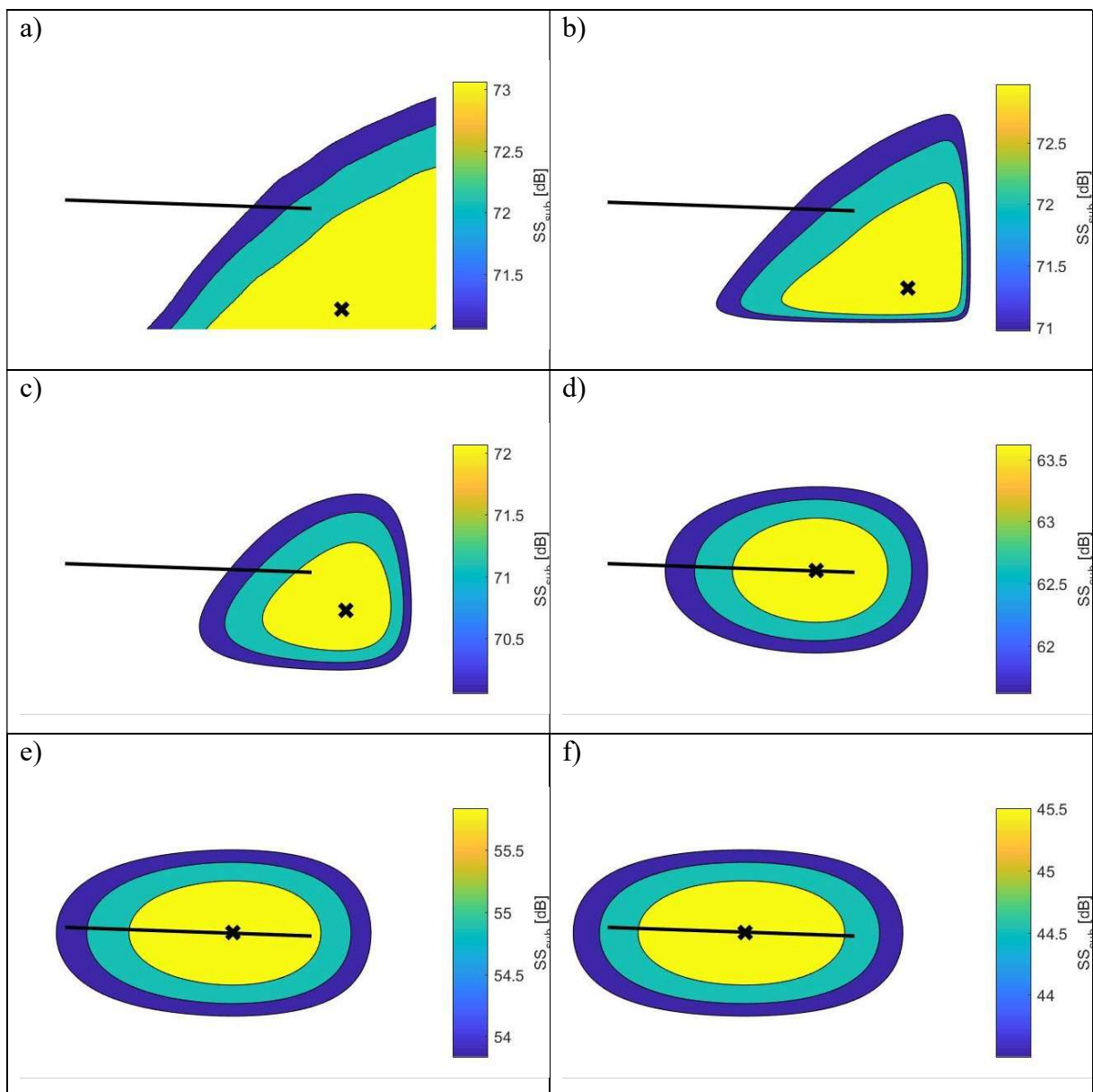
*Figure 4. Phases of filtering for the RAF6-E airfoil at Re= 100 000 and α=2°. **Underfiltering**: a) n = 0 and b) n = 100; **optimum filtering**: c) n = 1000; **overfiltering**: d) n = 10 000 and e) n = 20 000 and **fully overfiltered**: f) n = 35 400.*

4   RESULTS

Beamforming maps were created not only at the frequencies, where signs of vortex shedding were found according to the hot-wire measurements, but also at double frequencies. The root mean square of the velocity fluctuation spectra of the hot-wire measurements showed peaks, with lower intensity compared to the single frequency, at double frequencies of the identified vortex shedding frequencies. Signs of vortex shedding at double frequencies also appeared in the works of [3, 7, 17] and [18]. At double frequencies the intensity level is lower, however the resolution of the PAM measurements becomes better, as it is inversely proportional to the frequency. Thus, investigations at double frequencies offer a potential for noise source identifying and localization as well. The intensity and the position of the peaks were gathered. The cases representing meaningful results from an aeroacoustic point of view are summarized in Table 2 and Table 3, and were examined in more detail. f_{PAM} corresponds to the frequency where beamforming maps were created. f_{TEVS} and f_{PVS} indicate the frequencies, where signs of trailing edge vortex shedding and profile vortex shedding were found, respectively. Δf is the frequency bandwidth of the beamform maps, which were determined in accordance with the hot-wire measurements [11]. The position of the peaks, with their values are shown in Figure 5 and Figure 6, for the trailing edge bluntness vortex shedding (TEVS) and the profile vortex shedding (PVS), respectively. Comparable measurement pairs were created from the results, and are numbered in the left column. An illustrative example, representing the capabilities of the proposed method, including the spatial confinement to the ROI, the background subtraction, the boundary conditioning and the Laplacian filtering is presented in Figure 7.

Table 2. Cases with trailing edge bluntness noise according to the hot-wire and PAM measurements

Profile	Re [-]	α [°]	f_{PAM} [Hz]	Δf [Hz]	$SS_{sub,max}$ [dB]
Flat plate	60 000	0	f_{TEVS}=660	20	58.0
			$2 \cdot f_{TEVS}$=1320	40	49.5
		2	f_{TEVS}=670	20	59.5
			$2 \cdot f_{TEVS}$=1340	40	49.0
		4	f_{TEVS}=650	20	59.5
		6	f_{TEVS}=620	40	62.0
			$2 \cdot f_{TEVS}$=1240	80	51.0
	100 000	2	f_{TEVS}=1240	30	61.0
		4	f_{TEVS}=1180	30	58.0
	140 000	2	$2 \cdot f_{TEVS}$=3410	60	66.5
		4	$2 \cdot f_{TEVS}$=3430	80	65.0
RAF6-E	60 000	0	f_{TEVS}=1200	50	49.5

Table 3. Cases with PVS noise according to the hot-wire and PAM measurements

Profile	Re [-]	α [°]	f_{PAM} [Hz]	Δf [Hz]	$SS_{sub,max}$ [dB]
Cambered plate	60 000	2	f_{PVS}=310	20	64.5
		4	f_{PVS}=290	20	63.5
	100 000	2	$2 \cdot f_{PVS}$=470	70	65.5
RAF6-E	60 000	0	f_{PVS}=390	10	66.0
			$2 \cdot f_{PVS}$=780	20	55.5
		4	$2 \cdot f_{PVS}$=380	400	62.0
	100 000	0	f_{PVS}=750	60	73.0
		2	f_{PVS}=770	40	72.0
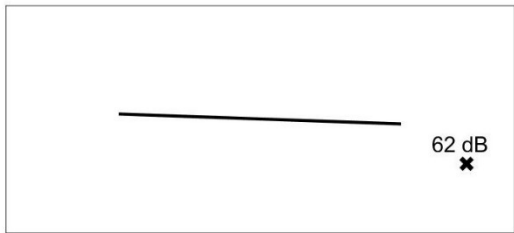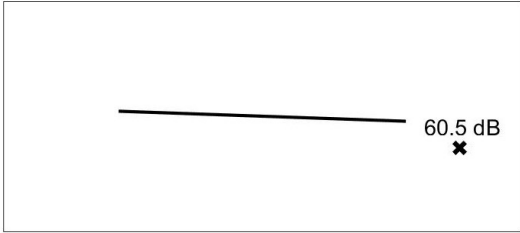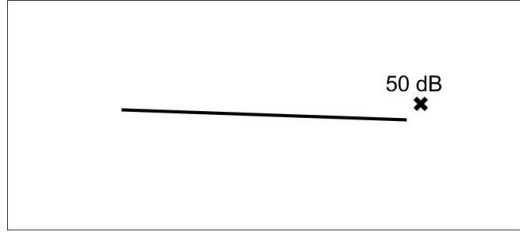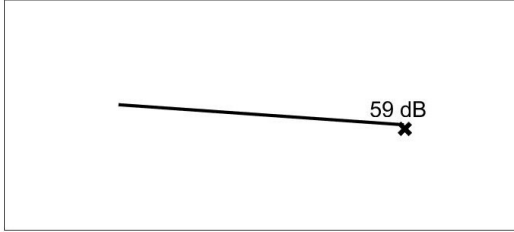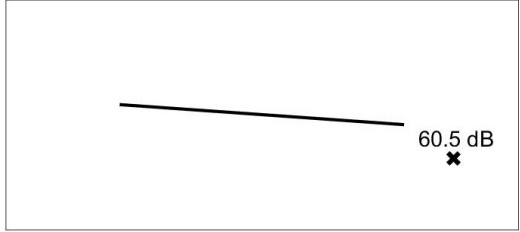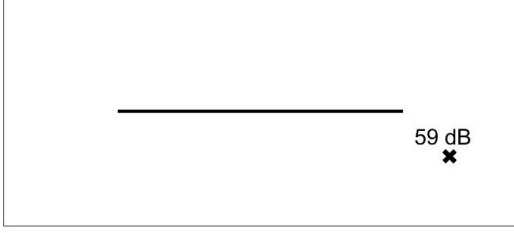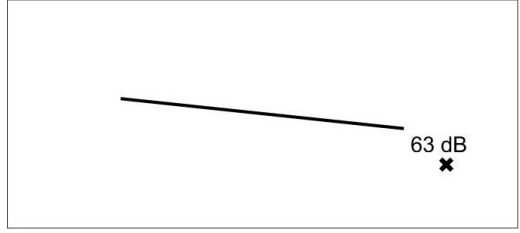
#	Datum PAM case	Compared PAM case
1	Flat plate, Re= 100 000, α=2°, f_{PAM}=f 62 dB	Flat plate, Re= 60 000, α=2°, f_{PAM} =f 60.5 dB
2	Flat plate, Re= 140 000, α=2°, f_{PAM} =$2 \cdot f$ 67.5 dB	Flat plate, Re= 60 000, α=2°, f_{PAM} =$2 \cdot f$ 50 dB
3	Flat plate, Re= 100 000, α=4°, f_{PAM} =f 59 dB	Flat plate, Re= 60 000, α=4°, f_{PAM} =f 60.5 dB
4	Flat plate, Re= 60 000, α=0°, f_{PAM} =f 59 dB	Flat plate, Re= 60 000, α=6°, f_{PAM} =f 63 dB

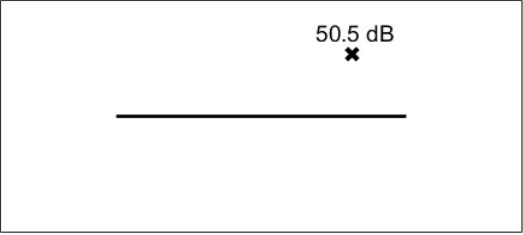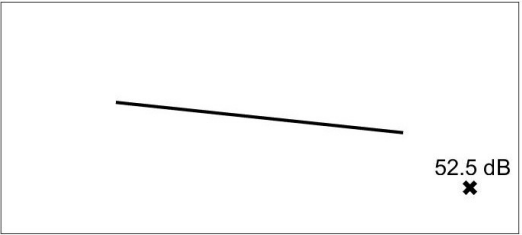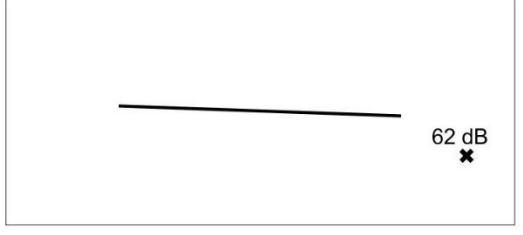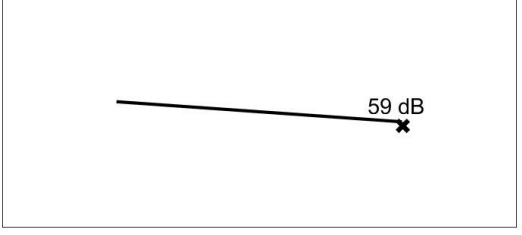*Figure 5. Detected peaks of the trailing edge bluntness vortex shedding (continued)*
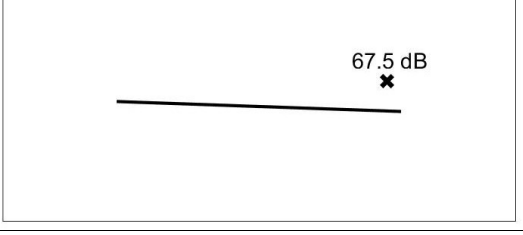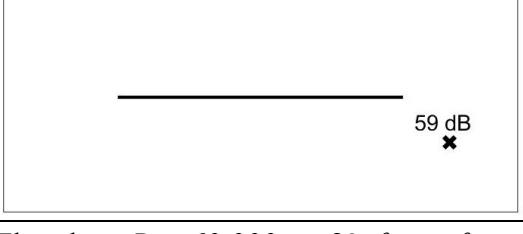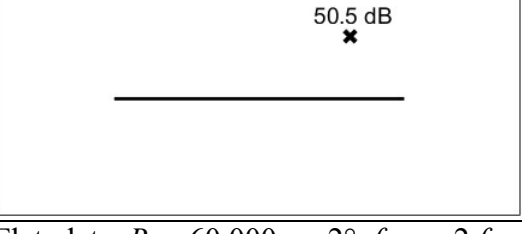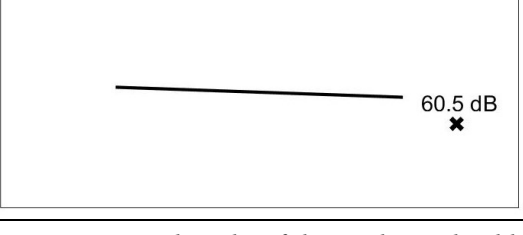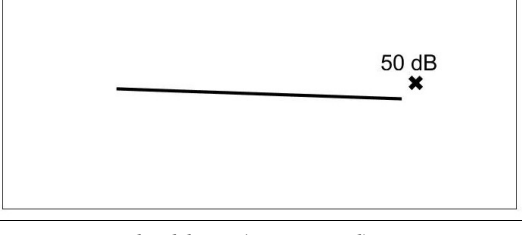
5	Flat plate, Re= 60 000, α=0°, f_{PAM} =2·f	Flat plate, Re= 60 000, α=6°, f_{PAM} =2·f
	50.5 dB ✖	52.5 dB ✖
6	Flat plate, Re= 100 000, α=2°, f_{PAM} =f	Flat plate, Re= 100 000, α=4°, f_{PAM} =f
	62 dB ✖	59 dB ✖
7	Flat plate, Re= 140 000, α=2°, f_{PAM} =2·f	Flat plate, Re= 140 000, α=4°, f_{PAM} =2·f
	67.5 dB ✖	66 dB ✖
8	Flat plate, Re= 60 000, α=0°, f_{PAM} =f	Flat plate, Re= 60 000, α=0°, f_{PAM} =2·f
	59 dB ✖	50.5 dB ✖
9	Flat plate, Re= 60 000, α=2°, f_{PAM} =f	Flat plate, Re= 60 000, α=2°, f_{PAM} =2·f
	60.5 dB ✖	50 dB ✖

Figure 5. Detected peaks of the trailing edge bluntness vortex shedding (continued)

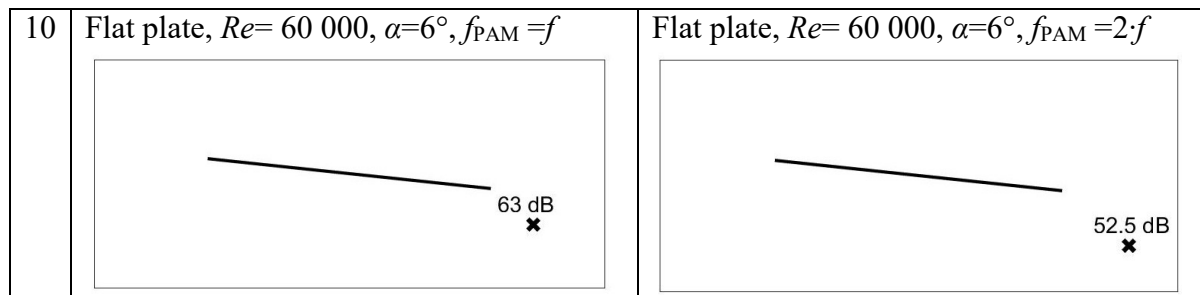| 10	Flat plate, *Re*= 60 000, α=6°, f_{PAM} =f	Flat plate, *Re*= 60 000, α=6°, f_{PAM} =2·f
	63 dB ✖	52.5 dB ✖

Figure 5. Detected peaks of the trailing edge bluntness vortex shedding (concluded)
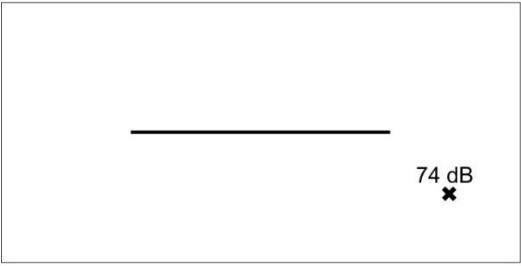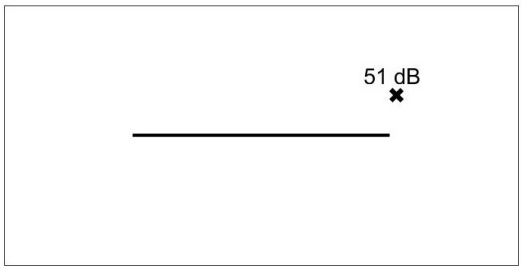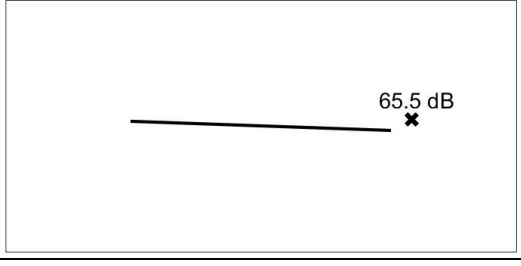
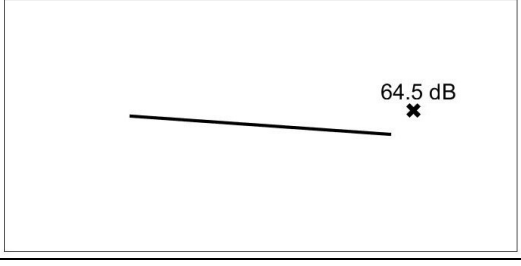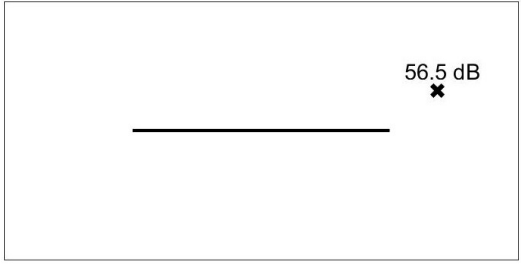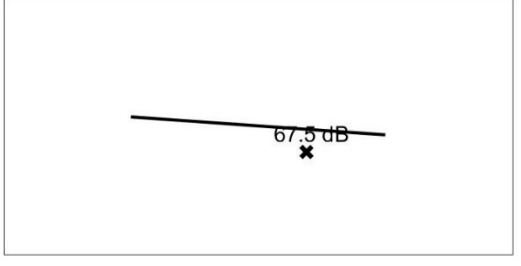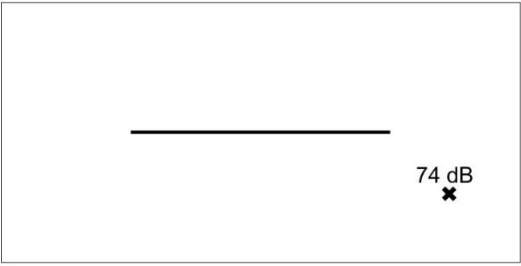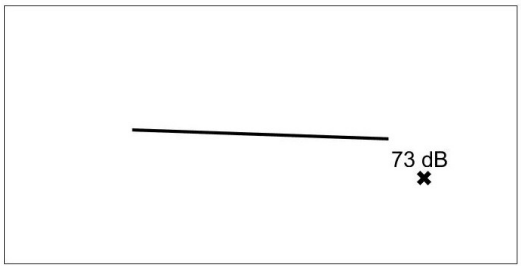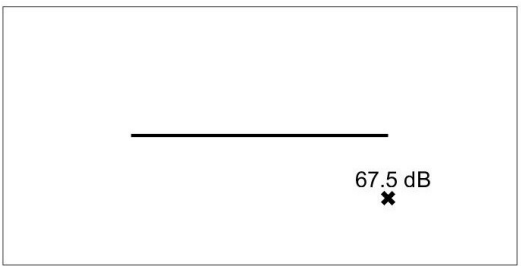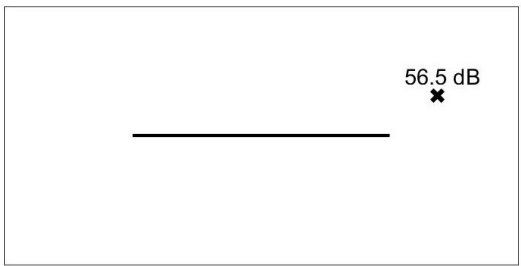| #	Datum PAM case	Compared PAM case
11	RAF6-E, Re= 100 000, α=0°, f_{PAM} =f 74 dB	RAF6-E, Re= 60 000, α=0°, f_{PAM} =f 51 dB
12	Cambered plate, Re= 60 000, α=2°, f_{PAM} =f 65.5 dB	Cambered plate, Re= 60 000, α=4°, f_{PAM} =f 64.5 dB
13	RAF6-E, Re= 60 000, α=0°, f_{PAM} =2·f 56.5 dB	RAF6-E, Re= 60 000, α=4°, f_{PAM} =2·f 67.5 dB
14	RAF6-E, Re= 100 000, α=0°, f_{PAM} =f 74 dB	RAF6-E, Re= 100 000, α=2°, f_{PAM} =f 73 dB
15	RAF6-E, Re= 60 000, α=0°, f_{PAM} =f 67.5 dB	RAF6-E, Re= 60 000, α=0°, f_{PAM} =2·f 56.5 dB

Figure 6. Detected peaks of the profile vortex shedding

Figure 7. Stages of processing: a) raw image, b) spatial confinement to ROI, c) boundary conditioning and background subtraction, d) final result after Laplacian filtering

According to the literature, both the trailing edge bluntness noise and the PVS noise obey the following trends. The noise intensity increases with the wind speed [3], proportionally with U_0^5 and $U_0^{5.5}$, in the case of trailing edge bluntness and profile vortex shedding, respectively. Furthermore the intensity decreases with the angle of attack [2, 3] and the frequency [3, 7, 17, 18]. By the evaluation o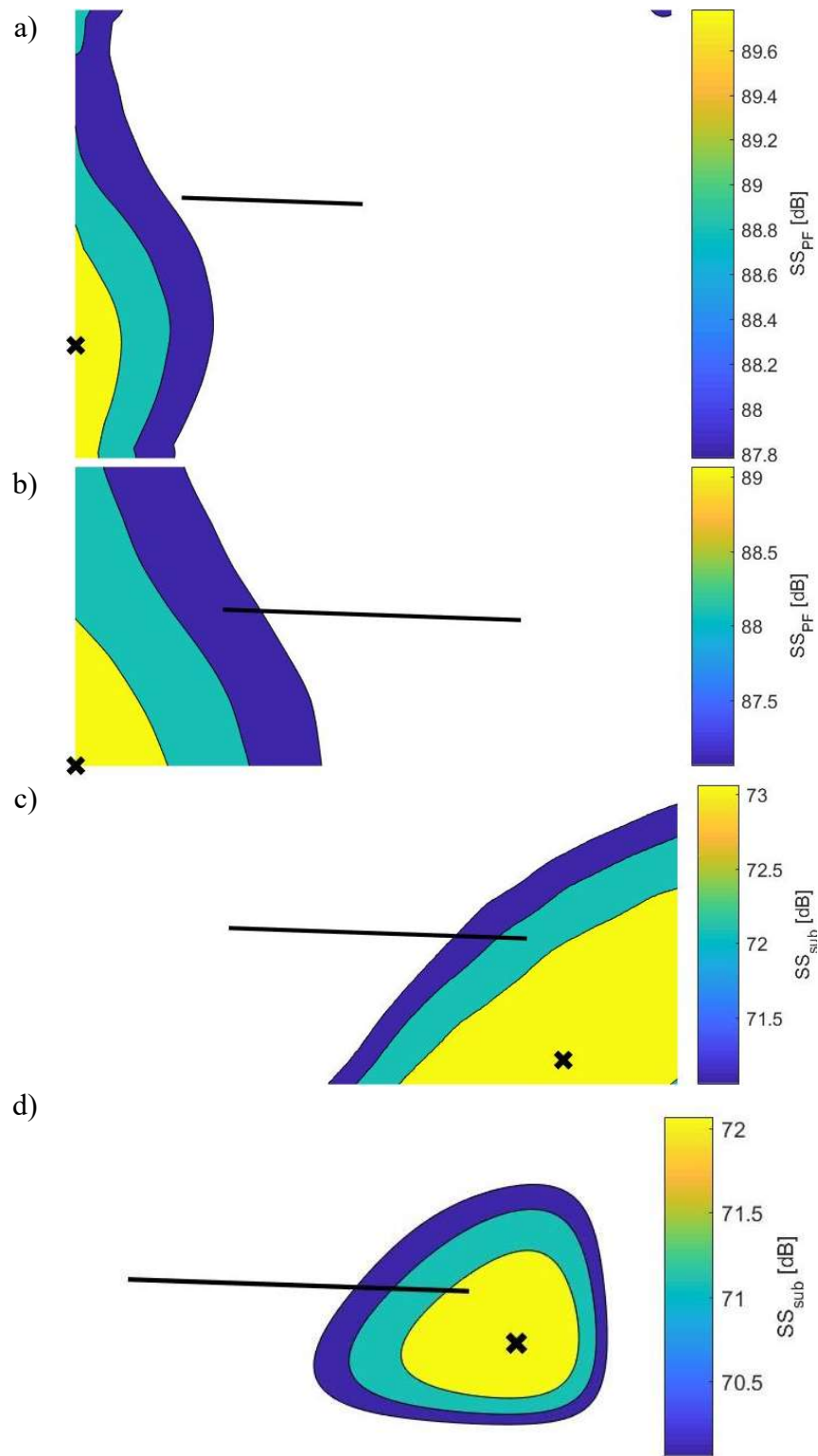f the comparable cases, presented in Figure 5 and Figure 6, and quantified in Table 4, where SPL stands for sound pressure level, the following trends can be stated for the measurements:

- The velocity dependence is met qualitatively for all cases, except for one, where the compared PAM case is at *Re* = 60 000. Quantitatively, if the prescribed intensity value is calculated from the higher velocity, the maximum deviation from the prescribed value is 10.5 dB.
- The angle of attack dependence is met for most of the cases. The off-trend cases are amongst the measurements at *Re* = 60 000, which are corrupted by measurement uncertainties the most.
- The frequency dependency is met for all cases.

Based on the above it can be concluded that the comparable cases, which include results at *Re* = 100 000 or 140 000, all meet the trends established in the literature, qualitatively.

In order to judge the localization capabilities of the PAM technique, calculations were performed including the trailing edge bluntness noise, of known position. The average deflection from the trailing edge was calculated in both the streamwise and transversal directions. The sample standard deviation of the deflections was also determined. The average deflections and the sample standard deviation of the deflections are shown in *Table 5*, where $\overline{\Delta x}/c$ and $\overline{\Delta z}/c$ are the relative average deflections in the streamwise and transversal directions respectively, and σ_x/c and σ_z/c are the relative sample standard deviation of the deflections in the streamwise and transversal directions, respectively. The resolution of the PAM technique calculated according to the Rayleigh criterion [19], λ/c is also included in Table 5. The position, where the profile bluntness noise is localized in average, along with the standard deviation is shown in Figure 8. The average location is denoted with the black cross, and the standard deviation is represented by the red ellipse.

From the results it can be seen that there is an insignificant amount of offset in the localization of the trailing edge bluntness noise. The standard deviations in the two directions are approximately the same. The localization capabilities of the method are an order of magnitude better, compared to that, determined with the Rayleigh criterion [19]. This means that even at such low frequencies the method is capable of localizing the trailing edge bluntness vortex shedding noise with high fidelity. For the location of the PVS noise the conclusion can be made, that the vortices may be initiated far upstream of the trailing edge. Despite this fact, the dominant noise, related to PVS tends to appear in the vicinity of the trailing edge.

Table 4. Validation of the PAM-based experimental evaluation technique, on the basis of quantitative and qualitative data (continued)

a) Item number	b) Phenomenon	c) Datum PAM case	d) PAM datum quantity	e) Reference	f) Trend in reference	g) Compared PAM case	h) Comparison of quantities: f →g based on f)	i) Comparison of quantities: f →g PAM
1	TEVS	Flat, $Re = 100\,000$, $\alpha = 2°$, $f_{PAM} = f$	62.0 dB	[3]	$SPL \sim U_0^{5.5}$	Flat, $Re = 60\,000$, $\alpha = 2°$, $f_{PAM} = f$	$\Delta SPL = -12$dB	$\Delta SS_{sub} = -1.5$dB
2	TEVS	Flat, $Re = 140\,000$, $\alpha = 2°$, $f_{PAM} = 2 \cdot f$	67.5 dB	[3]	$SPL \sim U_0^{5.5}$	Flat, $Re = 60\,000$, $\alpha = 2°$, $f_{PAM} = 2 \cdot f$	$\Delta SPL = -20$dB	$\Delta SS_{sub} = -17.5$dB
3	TEVS	Flat, $Re = 100\,000$, $\alpha = 4°$, $f_{PAM} = f$	59.0 dB	[3]	$SPL \sim U_0^{5.5}$	Flat, $Re = 60\,000$, $\alpha = 4°$, $f_{PAM} = f$	$\Delta SPL = -12$dB	$\Delta SS_{sub} = +1.5$dB
4	TEVS	Flat, $Re = 60\,000$, $\alpha = 0°$, $f_{PAM} = f$	59.0 dB	[2]	SPL decreases with α	Flat, $Re = 60\,000$, $\alpha = 6°$, $f_{PAM} = f$		$\Delta SS_{sub} = +4$dB
5	TEVS	Flat, $Re = 60\,000$, $\alpha = 0°$, $f_{PAM} = 2 \cdot f$	50.5 dB	[2]	SPL decreases with α	Flat, $Re = 60\,000$, $\alpha = 6°$, $f_{PAM} = 2 \cdot f$		$\Delta SS_{sub} = +2$dB
6	TEVS	Flat, $Re = 100\,000$, $\alpha = 2°$, $f_{PAM} = f$	62.0 dB	[2]	SPL decreases with α	Flat, $Re = 100\,000$, $\alpha = 4°$, $f_{PAM} = f$		$\Delta SS_{sub} = -3$dB
7	TEVS	Flat, $Re = 140\,000$, $\alpha = 2°$, $f_{PAM} = 2 \cdot f$	67.5 dB	[2]	SPL decreases with α	Flat, $Re = 140\,000$, $\alpha = 4°$, $f_{PAM} = 2 \cdot f$		$\Delta SS_{sub} = -1.5$dB
8	TEVS	Flat, $Re = 60\,000$, $\alpha = 0°$, $f_{PAM} = f$	59.0 dB	[3] [7] [17] [18]	SPL decreases with f	Flat, $Re = 60\,000$, $\alpha = 0°$, $f_{PAM} = 2 \cdot f$		$\Delta SS_{sub} = -8.5$dB

Table 4. Validation of the PAM-based experimental evaluation technique, on the basis of quantitative and qualitative data (concluded)

No.	Type	Configuration	Value	Ref.	Qualitative	Configuration	ΔSPL	ΔSS_{sub}
9	TEVS	Flat, $Re = 60\,000$, $\alpha = 2°$, $f_{PAM} = f$	60.5 dB	[3] [7] [17] [18]	SPL decreases with f	Flat, $Re = 60\,000$, $\alpha = 2°$, $f_{PAM} = 2 \cdot f$		$\Delta SS_{sub} = -10.5\text{dB}$
10	TEVS	Flat, $Re = 60\,000$, $\alpha = 6°$, $f_{PAM} = f$	63.0 dB	[3] [7] [17] [18]	SPL decreases with f	Flat, $Re = 60\,000$, $\alpha = 6°$, $f_{PAM} = 2 \cdot f$		$\Delta SS_{sub} = -10.5\text{dB}$
11	PVS	RAF6-E, $Re = 100\,000$, $\alpha = 0°$, $f_{PAM} = f$	74.0 dB	[3]	$SPL \sim U_0^5$	RAF6-E, $Re = 60\,000$, $\alpha = 0°$, $f_{PAM} = f$	$\Delta SPL = -11\text{dB}$	$\Delta SS_{sub} = -6.5\text{dB}$
12	PVS	Cambered, $Re = 60\,000$, $\alpha = 2°$, $f_{PAM} = f$	65.5 dB	[2]	SPL decreases with α	Cambered, $Re = 60\,000$, $\alpha = 4°$, $f_{PAM} = f$		$\Delta SS_{sub} = -1\text{dB}$
13	PVS	RAF6-E, $Re = 60\,000$, $\alpha = 0°$, $f_{PAM} = 2 \cdot f$	56.5 dB	[3]	SPL decreases with α	RAF6-E, $Re = 60\,000$, $\alpha = 4°$, $f_{PAM} = 2 \cdot f$		$\Delta SS_{sub} = +11\text{dB}$
14	PVS	RAF6-E, $Re = 100\,000$, $\alpha = 0°$, $f_{PAM} = f$	74.0 dB	[3]	SPL decreases with α	RAF6-E, $Re = 60\,000$, $\alpha = 2°$, $f_{PAM} = 2 \cdot f$		$\Delta SS_{sub} = -1\text{dB}$
15	PVS	RAF6-E, $Re = 60\,000$, $\alpha = 0°$, $f_{PAM} = f$	67.5 dB	[3] [7] [17] [18]	SPL decreases with f	RAF6-E, $Re = 60\,000$, $\alpha = 0°$, $f_{PAM} = 2 \cdot f$		$\Delta SS_{sub} = -11\text{dB}$

Table 5. Average deflection of the position of the localized noise sources from the trailing edge of the profiles, and the sample standard deviation of the deflections in the streamwise and transversal directions

	$\overline{\Delta x}$ /c [%]	$\overline{\Delta z}$ /c [%]	σ_x /c [%]	σ_z /c [%]	λ/c [%]
Trailing edge bluntness	-9	-3	12	13	160
Profile vortex shedding	-6	-6	15	13	349

Figure 8. The average position of the detected trailing edge bluntness vortex shedding noise, with the indication of the standard deviation

5   SUMMARY

A novel beamforming map processing method had been proposed, based on the Laplacian filtering technique. In order to validate the method, phased array microphone measurements had been concluded in a wind tunnel, on axial fan blade sections. The measurements were performed at moderate Reynolds numbers, Re = 60 000-140 000, which is characteristic of low-speed axial fans. The investigated profiles included a flat plate, a cambered plate and a RAF6-E profile. The results show that the method is capable of localizing vortex shedding noise in environments contaminated with extensive levels of background noise. The peak levels are qualitatively in accordance with the trends proposed in the literature.

In the future the method could further be validated with simulations on artificial noise sources. The quality of the measurement results could be improved by using larger arrays, with better resolution at such low frequencies.

ACKNOWLEDGEMENT

REFERENCES

[1]   T. J. Mueller, "Aerodynamic measurements at low Reynolds numbers for fixed wing micro-air vehicles," in RTO AVT/VKI Special Course, Development and operation of UAVs for military and civil applications, VKI, Belgium, 13-17 September 1999

[2]   M. Roger and S. Moreau, "Extensions and limitations of analytical airfoil broadband noise models," International Journal of Aeroacoustics, vol. 9, pp. 273-305, 2010.

[3]   T. F. Brooks, D. S. Pope and M. A. Marcolini, "Airfoil Self-Noise and Prediction," NASA Ref. Publication 1218, 1989.

[4]   H. Dou, Z. Li, P. Lin, Y. Wei, Y. Chen, W. Cao and H. He, "An improved prediction model of vortex shedding noise from blades of fans," *Journal of Thermal Science,* vol. 25, no. 6, pp. 526-531, 2016.

[5]   E. Balla and J. Vad, "A semi-empirical modell for predicting the frequency of profile vortex shedding relevant to low-speed axial fan blade sections," in The 13th European Conference on Turbomachinery Fluid Dynamics and Thermodynamics, Lausanne, Switzerland, Paper ID: 311, 12p., 8-12 April 2019

[6]   T. Carolus, Ventilatoren, Wiesbaden: B. G. Teubner Verlag, 2003.

[7]   S. Yarusevych, P. E. Sullivan and J. G. Kawall, "On vortex shedding from an airfoil in low-Reynolds-number flows," Journal of Fluid Mechanics, vol. 632, pp. 245-271, 2009.

[8]   Y. Diamant and Y. Schechner, "Overcoming Visual Reverberations," in Proc. IEEE Computer Vision and Pattern Recognition, Anchorage, AK, USA, 2008.

[9]   Y. Tian and S. Narasimhan, "Seeing through water: Image restoration using model-based tracking," in IEEE 12th International Conference on Computer Vision, Kyoto, Japan, 2009.

[10]   R. C. Gonzalez and R. E. Woods, Digital Image Processing, 2nd ed., Upper Saddle River, New Jersey: Prentice Hall, 2002.

[11]   G. Daku and J. Vad, "Experiment-based preliminary design guidelines for consideration of profile vortex shedding from low-speed axial fan blades," in *Proc. ASME Turbo Expo 2020*, London, UK, Paper ID: GT2020-14214, June 22-26, 2020.

[12]   Balla E, Vad J. Lift and drag force measurements on basic models of low-speed axial fan blade sections, *Proc IMechE, Part A: J Power and Energy* 2019 233(2) 165-175.

[13]   E. Balla and J. Vad, "Combined aerodynamic and phased array microphone studies on basic models of low-speed axial fan blade sections," in ASME Turbo Expo 2018: Turbomachinery Technical Conference and Exposition, Oslo, Norway, Paper Id: GT2018-75778, p. 11, 11-15 June 2018.

[14]   P. Jordan, J. A. Fitzpatrick and J.-C. Valiére, "Measurement of an Aeroacoustic Dipole Using a Linear Microphone Array," The Journal of the Acoustical Society of America, vol. 111, pp. 1267-1273, 2001.

[15]   Y. Liu, A. R. Quayle, A. P. Dowling and P. Sijtsma, "Beamforming Correction for Dipole Measurement Using Two-Dimensional Microphone Arrays," The Journal of the Acoustical Society of America, vol. 124, pp. 182-191, 2008.

[16]   T. Benedek, "Axiális átömlésű ventilátor mikrofontömbös diagnosztikája," PhD dissertation, Budapest, 2017.

[17] A. S. Hersh, P. T. Sodermant and R. E. Hayden, "Investigation of acoustic effects of leading-edge serrations on airfoils," Journal of Aircraft, vol. 11, no. 4, pp. 197-202, 1974.

[18] R. W. Paterson, P. G. Vogt, M. R. Fink and C. L. Munch, "Vortex noise of isolated airfoils," Journal of Aircraft, vol. 10, no. 5, pp. 296-302, 1973.

[19] B. Tóth and J. Vad, "Algorithmic Localisation of Noise Sources in the Tip Region of a Low-Speed Axial Flow Fan," *Journal of Sound and Vibration,* vol. 393, pp. 425-441, 2017.